INORGANIC CHEMISTRY FRONTIERS

RESEARCH ARTICLE

View Article Online
View Journal | View Issue

Check for updates

Cite this: *Inorg. Chem. Front.*, 2024, **11**, 6135

Aerial carbon dioxide conversion to carbonate mediated by a lead(II) complex with tridentate bipyridine containing a hydrazide ligand under electrochemical conditions yielding single-component white-light-emitting phosphors†

Ghodrat Mahmoudi, [a,b,c] Isabel Garcia-Santos, *[d] Elena Labisbal,[d] Alfonso Castiñeiras, [d] Vali Alizadeh,*[e] Rosa M. Gomila, [f] Antonio Frontera *[f] and Damir A. Safin *[g,h]

A novel tetranuclear complex $[Pb_4L_4(CO_3)_2]\cdot 4H_2O$ (**1**·4H$_2$O) is reported, which was obtained through the electrochemical oxidation of a lead anode under an ambient atmosphere in a CH_3CN : MeOH solution of *N′*-isonicotinoylpicolinohydrazonamide (**HL**). CO_3^{2-} anions were formed through the conversion of aerial CO_2 *via* the Pb^{2+}–**L** complex system under electrochemical conditions. The ligand **L** links two Pb^{2+} cations through the carbonyl oxygen atom, while the CO_3^{2-} anion links two Pb^{2+} cations through two monodentate and one bidentate oxygen atoms. The molecular structure of **1** is stabilized by a pair of Pb···O tetrel bonds formed with the bidentate oxygen atom of the CO_3^{2-} anion, while molecules of **1** are interlinked through reciprocal π(chelate ring)···π(chelate ring), π(chelate ring)···π(noncovalent ring) and Pb···π(noncovalent ring) interactions, yielding a 1D supramolecular chain. The same reaction but under a nitrogen atmosphere yielded a novel mononuclear complex $[PbL_2]\cdot MeOH\cdot 2H_2O$ (**2**·MeOH·2H$_2$O). In the structure of **2**, each ligand L exhibits a tridentate coordination mode. Molecules of **2** are also interlinked through reciprocal π(chelate ring)···π(chelate ring), π(chelate ring)···π(noncovalent ring) and Pb···π(noncovalent ring) interactions, similar to **1**, yielding a 1D supramolecular chain. The energetic features of these assemblies were studied using DFT calculations. Additionally, QTAIM analysis was employed to characterize noncovalent contacts, including intermolecular Pb···N tetrel bonds. These tetrel bonds were further analyzed using the ELF and Laplacian of electron density 2D maps, which confirmed their noncovalent nature. The optical properties of the complexes were revealed using UV–vis and diffuse reflectance spectroscopy and spectrofluorometry. Both complexes were found to be emissive in a solution of MeOH. CIE-1931 chromaticity coordinates of (0.38, 0.37) and (0.31, 0.32) for **1**·4H$_2$O and **2**·MeOH·2H$_2$O, respectively, fall within the white gamut of the chromaticity diagram.

Received 27th May 2024,
Accepted 22nd July 2024

DOI: 10.1039/d4qi01323a

rsc.li/frontiers-inorganic

Open Access Article. Published on 23 July 2024. Downloaded on 1/21/2026 11:43:33 PM.
This article is licensed under a Creative Commons Attribution 3.0 Unported Licence.

1. Introduction

It is well known that carbon dioxide (CO_2) is the key contributor to global warming.[1–3] At the same time, CO_2 can be considered an abundant renewable resource for carbonate and hydrocarbon products with commercial value. However, the efficient fixation and activation of CO_2 still remain a challenge. The chemical activation of CO_2 with its further transformation

[a]*Department of Chemistry, Faculty of Science, University of Maragheh, P.O. Box 55136-83111 Maragheh, Iran*
[b]*Chemistry Department, Faculty of Engineering and Natural Sciences, Istinye University, Sariyer, Istanbul 34396, Turkey*
[c]*Western Caspian University, Istiqlaliyyat Street 31, AZ 1001, Baku, Azerbaijan*
[d]*Departamento de Química Inorgánica, Facultad de Farmacia, Universidad de Santiago de Compostela, E-15782 Santiago de Compostela, Spain. E-mail: isabel.garcia@usc.es*
[e]*Department of Petroleum Engineering, Faculty of Engineering, University of Garmsar, Garmsar, Iran. E-mail: va11180@yahoo.com*
[f]*Departament de Quimica, Universitat de les Illes Balears, Crta de valldemossa km 7.5, 07122 Palma de Mallorca, Baleares, Spain. E-mail: toni.frontera@uib.es*
[g]*University of Tyumen, Tyumen, 625003, Russian Federation. E-mail: damir.a.safin@gmail.com*
[h]*Scientific and Educational and Innovation Center for Chemical and Pharmaceutical Technologies, Ural Federal University named after the First President of Russia B.N. Yeltsin, Ekaterinburg, 620002, Russian Federation*

†CCDC 2257285 and 2355288. For crystallographic data in CIF or other electronic format see DOI: https://doi.org/10.1039/d4qi01323a

Open Access Article. Published on 23 July 2024. Downloaded on 1/21/2026 11:43:33 PM.
This article is licensed under a Creative Commons Attribution 3.0 Unported Licence.

to value-added carbon-containing compounds is, most likely, the most efficient way to solve this problem. Without doubt, nature has found the best way to convert CO_2 to carbohydrate molecules, such as sugars, using photosynthesis.[4,5] Since CO_2 is an inert and thermodynamically stable molecule, the most promising way to achieve its activation is catalysis. As such, the interaction between CO_2 and transition metals has attracted significant attention from scientists because of being the most powerful tool for activating inert molecules.[6–8] Both homogeneous and heterogeneous catalyses have actively been utilized for transition metal-mediated CO_2 activation and conversion.[6–8] Depending on experimental conditions, CO_2 can be reduced by series of electron and proton transfers to a variety of products: CO, carbonate, carbamate, methane, formaldehyde, formic acid, methanol or oxalic acid.[6–8] It has been suggested that the activation of CO_2 is influenced by its one-electron reduction with the formation of a highly active $CO_2^{\bullet-}$ radical anion. Experimentally, the reduction of CO_2 requires great negative potentials[9–11] because of the formation of high energy intermediates and the large reorganizational energy between the linear molecule and bent radical anion. Thus, the presence of metal complexes, as well as other experimental conditions, might change these potentials significantly and, hence, favor the activation of CO_2.

On the other hand, among the great variety of noncovalent interactions, which are a powerful tool to drive the crystal packing, the most prominent ones are, likely, hydrogen bonds[12–14] and π-stacking[15–17] interactions. About a decade and a half ago, the σ-hole concept was introduced.[18] Later on, both σ- and π-hole interactions were highly accepted as being one of the pivotal structure-dictating forces. Within the concept of these interactions, σ- and π-holes are electron-deficient regions localized on the atom (Lewis acid), which can interact with an electron-rich atom (Lewis base).

Among the many types of σ-hole interactions, tetrel bonding has also been investigated in many studies. This type of noncovalent interaction is formed by a group 14 atom acting as a Lewis acid.[19] The lead(II) cation (Pb^{2+}) seems to be of particular interest to form tetrel bonding due to both its variety of coordination numbers and large ionic radius. Furthermore, the $6s^2$ lone-pair in the Pb^{2+} cation can generate either hemi- or holodirectional coordination,[20–23] of which the former one can facilitate tetrel bonding, yielding the formation of supramolecular architectures with extended structures and unique properties.

With all this in mind and in continuation of our comprehensive studies on the coordination chemistry of hemidirected Pb^{2+} architectures as well in shedding light on the role of noncovalent interactions in the formation of extended structures,[24–39] we focused our efforts on *N'*-isonicotinoylpicolinohydrazonamide (**HL**),[40] which was intentionally designed to serve as a potential bridging ligand, in the reaction with lead as a complexing agent. Finally, to shed light on the nature of the Pb···N tetrel bonds observed in self-assembled supramolecular dimers of both compounds in the solid state, DFT calculations were used along with MEP surface and QTAIM analyses.

2. Results and discussion

Electrochemical oxidation of a lead anode under an ambient atmosphere in a solution of **HL** in a mixture of CH_3CN and MeOH allowed the production of the tetranuclear complex $[Pb_4L_4(CO_3)_2]\cdot 4H_2O$ (**1**·4H_2O), which was obtained as yellow prism-like crystals, suitable for X-ray studies, by slow evaporation of the resulting solution. The same reaction but under a nitrogen atmosphere allowed obtaining the novel mononuclear complex $[PbL_2]\cdot MeOH\cdot 2H_2O$ (**2**·MeOH·2H_2O) as orange needle-like crystals also suitable for X-ray studies. Thus, aerial CO_2 was converted to carbonate by the Pb^{2+}–**L** complex system under electrochemical conditions.

The elemental analysis data fully supported the composition of the isolated metallocomplexes. Comparison of the FTIR spectra of the parent ligand **HL** and the complexes revealed the absence of a band for the NH(C═O) group, which was shown at 3385 cm^{-1} in the spectrum of **HL** (Fig. 1), verifying its deprotonation upon coordination. Furthermore, the presence of the CO_3^{2-} anions in the structure of complex **1**·4H_2O was supported by a broad band centred at about 1330 cm^{-1}, which partially overlapped with the bands from the ligand **L** (Fig. 1). The ^1H NMR spectra of the complexes recorded in DMSO-d_6 also supported the deprotonated form of the parent organic ligand in their structures, due to the absence of the peak for the amide hydrogen atom, which, in turn, was revealed in the ^1H NMR spectrum of **HL**, recorded in the same solvent, at 10.42 ppm (Fig. 1). Moreover, the signals for the pyridyl and NH_2 hydrogen atoms were remarkably

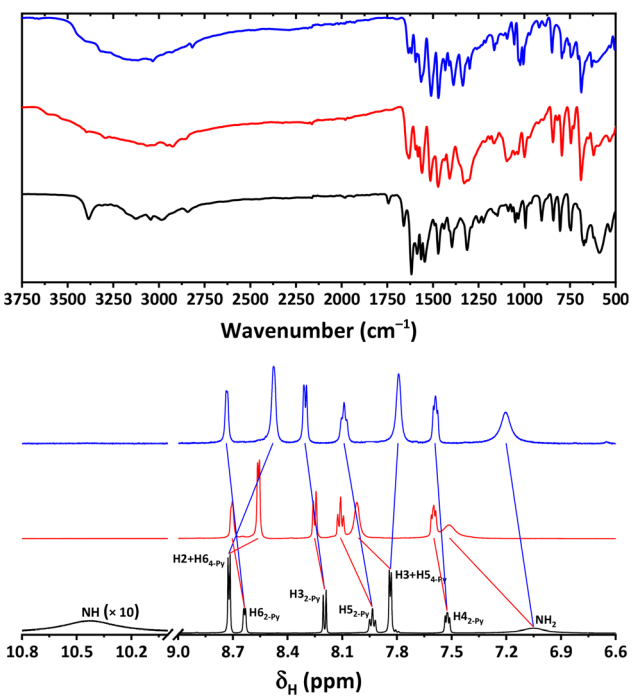

Fig. 1 IR (top) and ^1H NMR (bottom) spectra of **HL** (black),[40] **1**·4H_2O (red) and **2**·MeOH·2H_2O (blue).

This journal is © the Partner Organisations 2024

Open Access Article. Published on 23 July 2024. Downloaded on 1/21/2026 11:43:33 PM.
This article is licensed under a Creative Commons Attribution 3.0 Unported Licence.

shifted in the spectra of the complexes in comparison to in the spectrum of HL[40] due to the complex formation (Fig. 1).

The absorption spectra of complexes **1**·4H_2O and **2**·MeOH·2H_2O in MeOH contained bands up to about 450 and 500 nm, respectively (Fig. 2). The diffuse reflectance spectra of the same complexes contained bands up to about 540 and 600 nm, respectively (Fig. 2). The corresponding experimental, direct and indirect band gap values for both complexes were very similar and varied from 2.29 to 2.42 eV and from 2.18 to 2.38 eV for **1**·4H_2O and **2**·MeOH·2H_2O, respectively (Fig. 2).

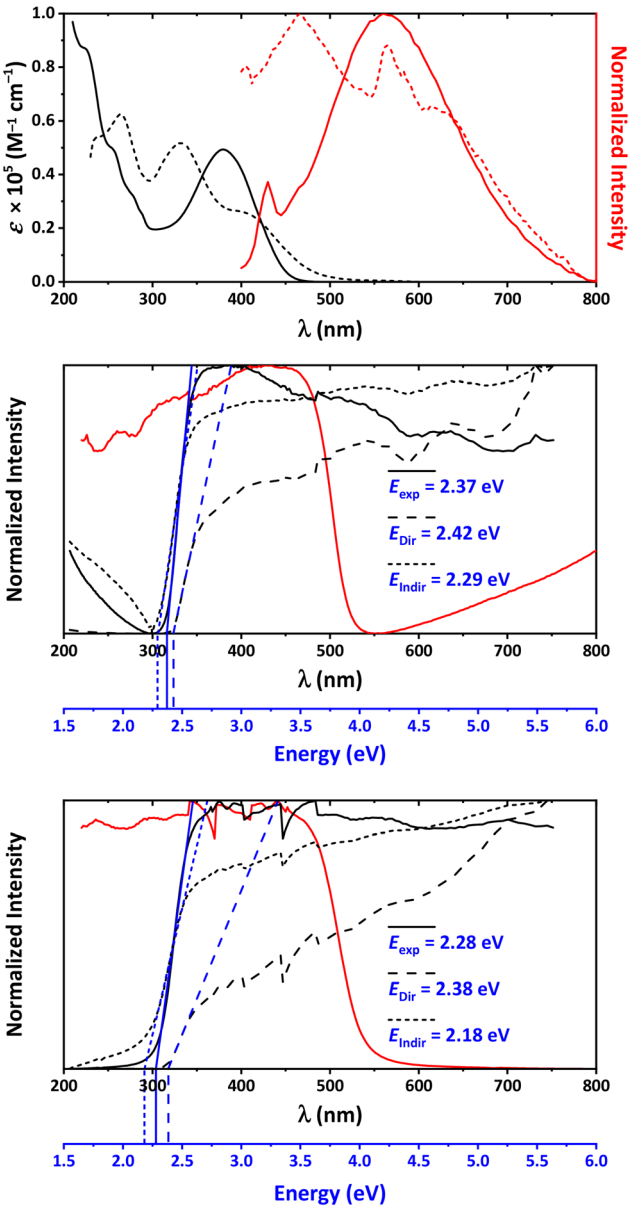

Fig. 2 (Top) UV–Vis (black) and luminescence (red) spectra of **1**·4H_2O (solid line) and **2**·MeOH·2H_2O (dashed line) recorded in MeOH. (Middle and bottom) Kubelka–Munk (red and black solid lines), $(\alpha h\nu)^2$ (dashed line) and $(\alpha h\nu)^{1/2}$ (short dashed line) spectra of **1**·4H_2O (middle) and **2**·MeOH·2H_2O (bottom).

The most striking finding was that the discussed complexes were found to be emissive in a solution of MeOH upon excitation at 375 and 330 nm, respectively, with a broad band from about 400 nm to 800 nm (Fig. 2). For complex **1**·4H_2O, the emission band exhibited a maximum at about 560 nm, while for complex **2**·MeOH·2H_2O, the emission band exhibited two clearly defined maxima at about 465 and 565 nm, of which the latter one was accompanied with a shoulder at about 625 nm (Fig. 2). The CIE-1931 chromaticity coordinates of (0.38, 0.37) and (0.31, 0.32) for **1**·4H_2O and **2**·MeOH·2H_2O, respectively, fall within the white gamut of the chromaticity diagram (Fig. 3). Thus, both complexes are single-component white light-emitting phosphors.

Complex **1**·4H_2O crystallized in the monoclinic space group *I*2/*a* with the $[Pb_2L_2(CO_3)]$ species and two molecules of water in the asymmetric unit cell. The molecule of **1** is constructed from two dinuclear cations $[Pb_2L_2]^{2+}$, which are, in turn, formed by two $[PbL]^+$ cations, where each metal cation is chelated by the tridentate ligand **L** through the 2-pyridyl and imine nitrogen atoms, and a carbonyl oxygen atom (Fig. 4). Two mononuclear cations $[PbL]^+$ are linked to a dimeric cation $[Pb_2L_2]^{2+}$ through the carbonyl oxygen atoms, which thus exhibit a bidentate bridging coordination mode (Fig. 4). Dinuclear cations $[Pb_2L_2]^{2+}$ are further interlinked through two carbonate anions, which, in turn, act as both bridging ligands and counterions, yielding a tetranuclear molecule $[Pb_4L_4(CO_3)_2]$ (Fig. 4). Each carbonate anion is symmetrically linked to two Pb^{2+} cations through all the oxygen atoms, of which two are monodentate and the third one exhibits a bridging bidentate coordination mode (Fig. 4). The metal cations

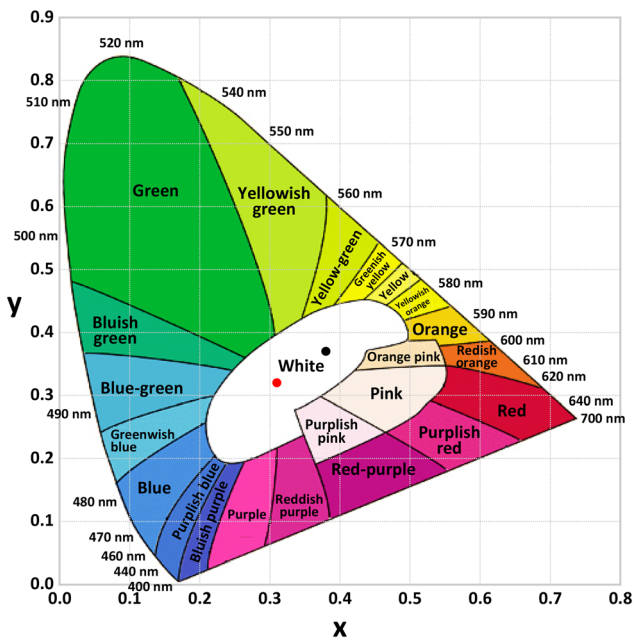

Fig. 3 CIE-1931 chromaticity diagram and the calculated CIE coordinates located at (0.38, 0.37) for **1**·4H_2O (black circle) and (0.31, 0.32) for **2**·MeOH·2H_2O (red circle).

Open Access Article. Published on 23 July 2024. Downloaded on 1/21/2026 11:43:33 PM. This article is licensed under a Creative Commons Attribution 3.0 Unported Licence.

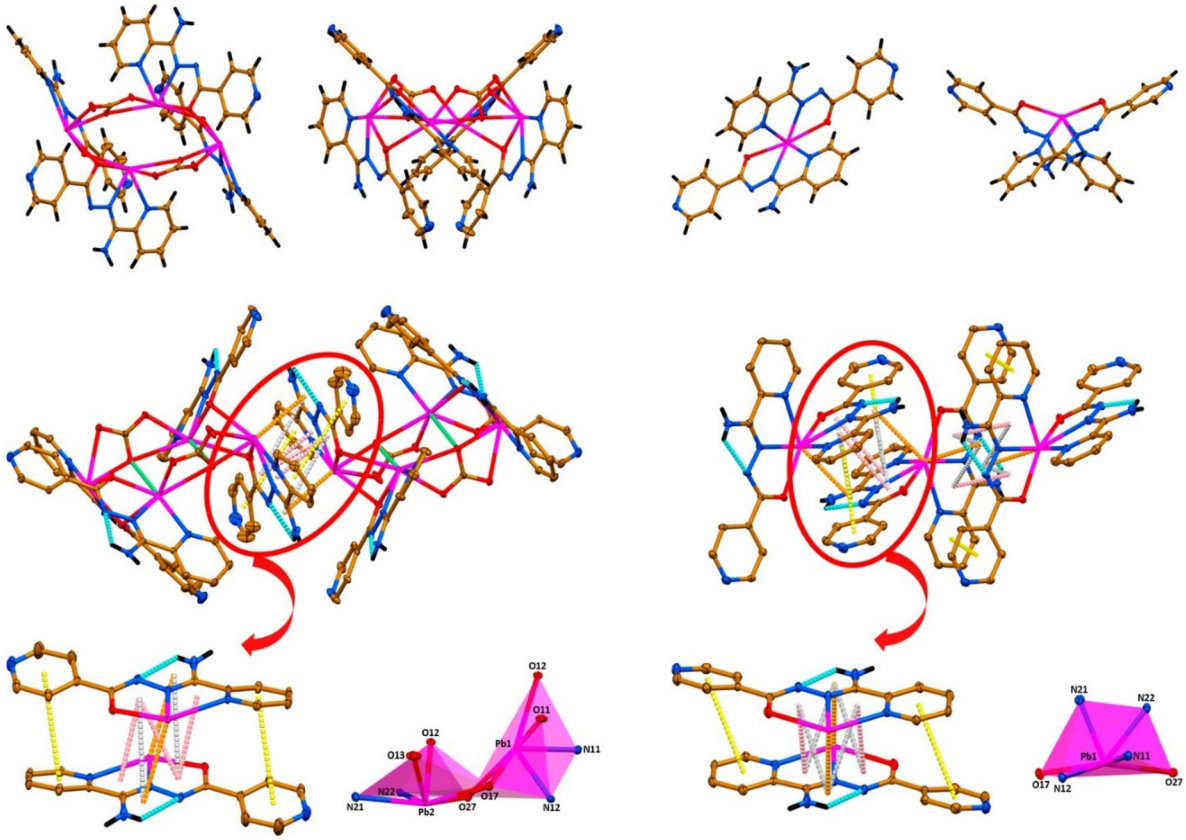

Fig. 4 (top) Different views of the molecular structures of **1** (left) and **2** (right). (Bottom) supramolecular interaction of molecules **1** (left) and **2** (right) through π(CR)···π(CR), π(CR)···π(NR), Pb···(NR) and π(2-Py)···π(4-Py) interactions (hydrogen atoms, except NH_2 groups, are omitted for clarity); and coordination polyhedra, formed by covalent bonds. Displacement ellipsoids are drawn with a 50% probability. Color code: H = black, C = gold, N = blue, O = red, Pb = magenta; N–H···N hydrogen bond = cyan dashed line, π(CR)···π(CR) interaction = pink dashed line, π(CR)···π(NR) = grey dashed line, Pb···(NR) = orange dashed line, and π(2-Py)···π(4-Py) interaction = yellow dashed line.

in the structure of **1** are in a six-membered N_2O_4 coordination environment, formed by covalent bonds. Notably, coordination of the deprotonated ligands **L** in the structure of **1** leads to some minor changes in the bond lengths (<0.06 Å) within the chelate fragments (Table 1) in comparison to those in the structure of the parent **HL**.[40]

The Pb–O bond lengths with the carbonyl oxygen atom of the same chelated ligand **L** are 2.377(2) and 2.394(2) Å, while the same bond lengths with the bridging carbonyl oxygen atom are significantly longer and vary from 2.815(2) to 2.911(2) Å (Table 1). The Pb–O distances with the monodentate and bridging carbonate atoms are 2.331(2) and 2.860(2) Å, respect-

Table 1 Selected bond lengths (Å) in the molecular structures of **1** and **2**

1[a]				**2**[b]			
$Pb1–O11_{carbonate}$	2.331(2)	C17–O17 (carbonyl)	1.300(4)	$Pb1–O17_{carbonyl}$	2.583(2)	N22–N23	1.408(3)
$Pb1–O12_{carbonate}$	2.860(2)	C16–N12 (imine)	1.333(4)	$Pb1–O27_{carbonyl}$	2.741(2)	Pb1···Cg3(NR)	3.337
$Pb1–O17_{carbonyl}$	2.377(2)	C17–N13 (amide)	1.304(4)	$Pb1–N11_{2\text{-}Py}$	2.595(3)	Pb1···Cg6(NR)	3.439
$Pb1–O27_{carbonyl}$	2.911(2)	N12–N13	1.393(4)	$Pb1–N21_{2\text{-}Py}$	2.609(3)		
$Pb1–N11_{2\text{-}Py}$	2.581(3)	C27–O27 (carbonyl)	1.276(4)	$Pb1–N12_{imine}$	2.479(2)		
$Pb1–N12_{imine}$	2.370(3)	C26–N22 (imine)	1.298(4)	$Pb1–N22_{imine}$	2.600(2)		
$Pb1···O12a_{carbonate}$	3.214(2)	C27–N23 (amide)	1.321(5)	C17–O17 (carbonyl)	1.282(3)		
$Pb2–O12_{carbonate}$	2.295(2)	N22–N23	1.396(4)	C27–O27 (carbonyl)	1.276(3)		
$Pb2–O13_{carbonate}$	2.711(3)	C10–O11 (carbonate)	1.278(4)	C16–N12 (imine)	1.303(4)		
$Pb2–O17a_{carbonyl}$	2.815(2)	C10–O12 (carbonate)	1.299(4)	C26–N22 (imine)	1.301(4)		
$Pb2–O27a_{carbonyl}$	2.394(2)	C10–O13 (carbonate)	1.272(4)	C17–N13 (amide)	1.331(4)		
$Pb2–N11a_{2\text{-}Py}$	2.655(3)	Pb2···Cg3(NR)	3.491	C27–N23 (amide)	1.326(4)		
$Pb2–N12a_{imine}$	2.401(3)			N12–N13	1.403(3)		

[a] Cg3(NR): N23–N22–C26–N26–H26B. [b] Cg3(NR): N13–N12–C16–N16–H16B; Cg6(NR): N23–N22–C26–N26–H26A.

 This journal is © the Partner Organisations 2024

Open Access Article. Published on 23 July 2024. Downloaded on 1/21/2026 11:43:33 PM. This article is licensed under a Creative Commons Attribution 3.0 Unported Licence.

ively, for the Pb1 metal atom, while the same distances for the Pb2 atom exhibit an opposite trend and 2.711(3) and 2.295(2) Å, respectively. The Pb–N bonds formed with the 2-pyridyl nitrogen atoms are 2.581(3) and 2.655(3) Å, while the same bonds with the imine nitrogen atoms are about 0.21–0.25 Å shorter (Table 1).

The most striking thing is that the molecular structure of **1** is stabilized by two Pb···O tetrel bonds of 3.214(2) Å formed between the Pb1 cations and the bridging carbonate oxygen atoms (Fig. 4 and Table 1). Furthermore, the molecules **1** are interlinked through reciprocal π(chelate ring, CR)···π(chelate ring, CR), π(chelate ring, CR)···π(noncovalent ring, NR), and Pb2···π(noncovalent ring, NR) interactions, yielding a 1D supramolecular chain (Fig. 4 and Tables 1 and 2), which is further strengthened by reciprocal π(2-Py)···π(4-Py) interactions formed between the 2- and 4-pyridyl fragments of the ligands **L**, which chelate the Pb2 cations (Fig. 4 and Table 2). Notably, the five-membered NR, formed by N26–H26B···N23 hydrogen bonding between one of the NH_2 hydrogen atoms and the amide nitrogen atom (Table 2), is pseudo-aromatic, as evidenced from the corresponding aromaticity index of 0.759, calculated from the HOMHED.[41] This value is higher than those of furans and (is)oxazoles.[41] The 1D supramolecular chains are linked by the reciprocal N16–H16A···O11 hydrogen bonds and additional π(2-Py)···π(4-Py) interactions (Table 2). Furthermore, molecules of water also serve as a "glue" between the supramolecular chains due to the formation of O–H···O, O–H···N, and N–H···O hydrogen bonds (Table 2).

Complex **2**·MeOH·2H_2O crystallized in the monoclinic space group $P2_1/n$ with one [PbL_2], one methanol, and two water molecules in the asymmetric unit cell. In the structure of **2**, each ligand L exhibits a tridentate coordination mode, yielding a six-membered N_4O_2 coordination environment (Fig. 4). Similar to the structure of **1**, coordination of the deprotonated ligands **L** in the structure of **2** leads to very minor changes in the bond lengths (<0.05 Å) within the chelate fragments (Table 1) in comparison to those in the structure of the parent **HL**.[40]

The Pb–$N_{2\text{-Py}}$, Pb–N_{imine}, and Pb–$O_{carbonyl}$ bond lengths with the coordinated sites of the same chelated ligand **L** are 2.595(3), 2.479(2), and 2.583(2) Å, respectively, with the shortest value observed for the bond with the imine nitrogen atom, while the other two coordination bonds are quite similar (Table 1). The same bonds formed with the coordination sites

Table 2 Hydrogen bond and π···π interaction lengths (Å) and angles (°) in the crystal structures of **1**·4H_2O and **2**·MeOH·2H_2O

1·4H_2O[a]					**2**·MeOH·2H_2O[b]				
D–X···A	*d*(D–X)	*d*(X···A)	*d*(D···A)	∠(DXA)	D–X···A	*d*(D–X)	*d*(X···A)	*d*(D···A)	∠(DXA)
O1–H1A···O13^{i}	0.93	1.75	2.643(5)	160	O1–H1···O3^{i}	0.96	1.73	2.684(3)	172
O1–H1B···N14^{ii}	0.95	2.41	3.272(4)	151	O2–H2A···O1^{ii}	0.80	2.04	2.804(4)	159
O2–H2A···O13^{i}	0.87	2.31	3.100(4)	151	O2–H2B···N14^{iii}	0.83	1.93	2.757(3)	173
O2–H2A···O17^{iii}	0.87	2.53	3.138(4)	128	O3–H3A···O27^{iv}	0.86	1.86	2.702(3)	169
N16–H16A···N13	0.91	2.28	2.635(4)	103	O3–H3B···N24^{v}	0.81	1.96	2.758(3)	168
N26–H26B···N23	0.77	2.40	2.627(4)	99	N16–H16A···N13	0.78	2.33	2.622(4)	103
N16–H16A···O11^{iv}	0.91	2.09	2.851(4)	141	N26–H26A···N23	0.85	2.22	2.589(4)	106
N16–H16B···O2^{v}	0.84	2.16	2.967(4)	161	N16–H16A···O2^{v}	0.78	2.13	2.856(3)	154
N26–H26A···O1^{vi}	0.86	2.12	2.917(5)	154	N16–H16B···O3^{vi}	0.78	2.21	2.905(3)	150
					N26–H26B···O2^{vii}	0.81	2.34	3.120(4)	162
Cg1···Cg2	*d*(Cg1···Cg2)	*α*	*β*	*γ*	Cg1···Cg2	*d*(Cg1···Cg2)	*α*	*β*	*γ*
Py_{N11}···Py_{N14}^{iv}	3.649(2)	9.1(2)	17.1	26.2	Py_{N11}···Py_{N14}^{iii}	3.595(2)	7.98(13)	21.6	20.3
Py_{N14}···Py_{N11}^{iv}	3.649(2)	9.1(2)	26.2	17.1	Py_{N14}···Py_{N11}^{iii}	3.595(2)	7.98(13)	20.3	21.6
Py_{N21}···Py_{N24}^{iii}	4.252(2)	26.8(2)	23.5	46.9	Py_{N21}···Py_{N24}^{viii}	3.976(2)	14.56(14)	27.2	29.5
Py_{N24}···Py_{N21}^{iii}	4.252(2)	26.8(2)	46.9	23.5	Py_{N24}···Py_{N21}^{viii}	3.976(2)	14.56(14)	29.5	27.2
Cg1(CR)···Cg2(CR)^{iii}	3.432(2)	5.6(2)	18.7	19.7	Cg1(CR)···Cg2(CR)^{iii}	3.303(2)	7.52(14)	14.7	18.4
Cg2(CR)···Cg1(CR)^{iii}	3.432(2)	5.6(2)	19.7	18.7	Cg2(CR)···Cg1(CR)^{iii}	3.303(2)	7.52(14)	18.4	14.7
Cg2(CR)···Cg2(CR)^{iii}	3.624(2)	0.0(2)	26.6	26.6	Cg2(CR)···Cg2(CR)^{iii}	3.628(2)	0.00(14)	33.8	33.8
Cg2(CR)···Cg3(NR)^{iii}	4.094(2)	3.7(2)	39.6	39.0	Cg1(CR)···Cg3(NR)^{iii}	4.000(2)	5.10(14)	40.7	39.3
Cg3(NR)···Cg2(CR)^{iii}	4.094(2)	3.7(2)	39.3	37.7	Cg3(NR)···Cg1(CR)^{iii}	4.000(2)	5.10(14)	39.3	40.7
					Cg2(CR)···Cg3(NR)^{iii}	3.421(2)	8.85(14)	25.1	20.3
					Cg3(NR)···Cg2(CR)^{iii}	3.421(2)	8.85(14)	20.3	25.1
					Cg4(CR)···Cg5(CR)^{viii}	3.522(2)	1.06(14)	12.9	13.4
					Cg5(CR)···Cg4(CR)^{viii}	3.522(2)	1.06(14)	13.4	12.9
					Cg4(CR)···Cg6(NR)^{viii}	3.692(2)	5.59(14)	20.6	25.5
					Cg6(NR)···Cg4(CR)^{viii}	3.692(2)	5.59(14)	25.5	20.6
					Cg5(CR)···Cg6(NR)^{viii}	3.682(2)	5.99(14)	22.9	25.1
					Cg6(NR)···Cg5(CR)^{viii}	3.682(2)	5.99(14)	25.1	22.9

[a] Cg 1(CR): Pb2–N21–C25–C26–N22; Cg2(CR): Pb2–N22–N23–C27–O27; Cg3(NR): N23–N22–C26–N26–H26B. Symmetry code: (i) x, $1/2 - y$, $1/2 + z$; (ii) x, $1 + y$, z; (iii) $1/2 - x$, $1/2 - y$, $1/2 - z$; (iv) $-x$, $-y$, $-z$; (v) $-1/2 + x$, $-1/2 + y$, $-1/2 + z$; (vi) $1/2 + x$, $1 - y$, z. [b] Cg 1(CR): Pb1–N11–C15–C16–N12; Cg2(CR): Pb1–N12–N13–C17–O17; Cg3(NR): N13–N12–C16–N16–H16B; Cg4(CR): Pb1–N21–C25–C26–N22; Cg5(CR): Pb1–N22–N23–C27–O27; Cg6 (NR): N23–N22–C26–N26–H26A. Symmetry code: (i) x, y, z; (ii) $-1/2 + x$, $1/2 - y$, $1/2 + z$; (iii) $-x$, $1 - y$, $-z$; (iv) $1 + x$, y, z; (v) $1/2 - x$, $1/2 + y$, $1/2 - z$; (vi) $1 - x$, $1 - y$, $-z$; (vii) $1/2 - x$, $-1/2 + y$, $1/2 - z$; (viii) $-x$, $-y$, $-z$.

Open Access Article. Published on 23 July 2024. Downloaded on 1/21/2026 11:43:33 PM. This article is licensed under a Creative Commons Attribution 3.0 Unported Licence.

of the second ligand **L** are longer. In particular, while the Pb–$N_{2\text{-Py}}$ bond length is only 0.014 Å longer, the Pb–N_{imine} and Pb–$O_{carbonyl}$ bond lengths are 0.121 and 0.158 Å longer, respectively (Table 1). It should be noted that the Pb–$N_{2\text{-Py}}$ and Pb–$O_{carbonyl}$ bonds formed with the first ligand **L** are very similar, with a difference of about 0.012 Å, while for the second ligand **L**, the Pb–$N_{2\text{-Py}}$ and Pb–N_{imine} bonds are very similar, with a difference of about 0.009 Å (Table 1). Thus, the second ligand is more weakly bound to the cation compared to the first ligand.

The molecules of **2** are also interlinked through reciprocal π(CR)···π(CR), π(CR)···π(NR), and Pb1···π(NR) interactions, yielding a 1D supramolecular chain (Fig. 4 and Tables 1 and 2), which is further strengthened by reciprocal π(2-Py)···π(4-Py) interactions (Fig. 4 and Table 2). The five-membered NRs, formed by N16–H16A···N13 and N26–H26A···N23 hydrogen bonding between one of the NH_2 hydrogen atoms and the amide nitrogen atom (Table 2), are also pseudo-aromatic, as evidenced from the corresponding aromaticity indexes of 0.739 and 0.705, respectively, which are higher than those of furans and (is)oxazoles.[41] Finally, the 1D supramolecular chains are linked through the formation of O–H···O, O–H···N and N–H···O hydrogen bonds with the lattice solvent molecules (Table 2).

The theoretical study focused on analysing the self-assembled dimers represented in the lower part of Fig. 4, which are formed by a combination of multiple interactions. Initially, we computed the molecular electrostatic potential (MEP) surfaces of **1** and **2** to identify the nucleophilic and electrophilic regions. The MEP surface of **1** showed a minimum at the carbonate oxygen atoms (−75.3 kcal mol^{-1}) and a maximum at the NH_2 groups (56.5 kcal mol^{-1}) (Fig. 5). This distribution explains the formation of multiple O–H···O and N–H···O bonds (Table 2). Additionally, the MEP surface was significantly negative at the 4-pyridine nitrogen atoms (−47.1 kcal mol^{-1}), which engage in interactions with the co-crystallized water molecules. Furthermore, the MEP over the pyridine ring was negative (−25.4 kcal mol^{-1}), while it was positive over the Pb-coordinated 2-pyridine ring (5.6 kcal mol^{-1}), elucidating the formation of π(2-Py)···π(4-Py) interactions (Fig. 4). The MEP surface at the Pb atom was anisotropic and presented a region where the MEP was a local maximum (σ-hole), becoming evident when a reduced scale was applied (Fig. 5). The MEP value at the σ-hole was 12.1 kcal mol^{-1}.

The MEP surface of **2** showed a minimum at the 4-pyridine nitrogen atom (−44.6 kcal mol^{-1}) and a maximum at the NH_2 groups (56.3 kcal mol^{-1}). This distribution explains the formation of hydrogen bonds with the co-crystallized water molecules (Table 2). The MEP surface at the hydrazido oxygen atom was also large and negative (−41.4 kcal mol^{-1}), facilitating interactions with a water molecule. Like for **1**, the MEP over the 4-pyridine ring was negative (−16.3 kcal mol^{-1}), while it was positive over the Pb-coordinated 2-pyridine ring (10.4 kcal mol^{-1}), enabling the formation of π(2-Py)···π(4-Py) interactions (Fig. 4). The MEP at the Pb atom was anisotropic and presented a large region where the MEP was a local maximum (σ-hole), which became evident when a reduced scale was applied (Fig. 5). The MEP value at the σ-hole was 20.7 kcal mol^{-1}.

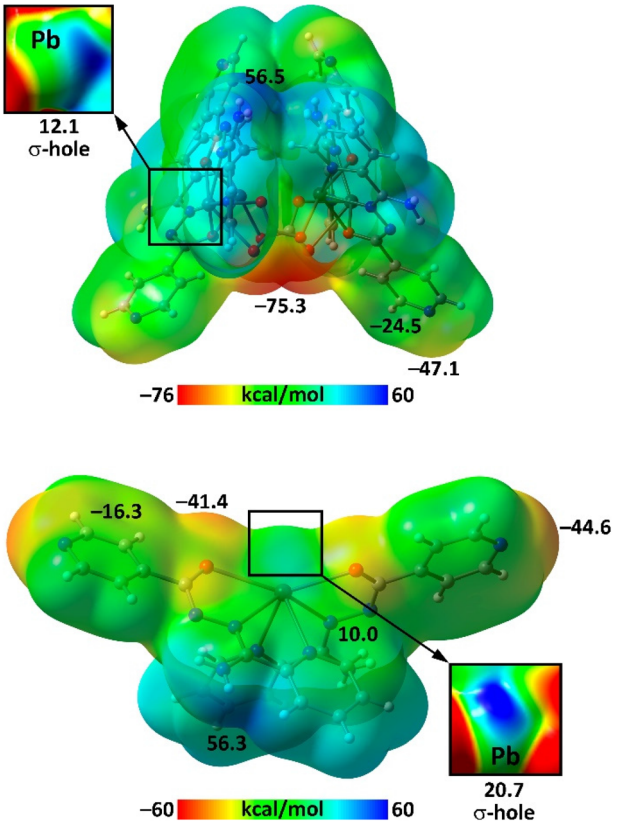

Fig. 5 MEP surfaces of **1** (top) and **2** (bottom).

Using quantum theory of atoms in molecules (QTAIM) analysis, we examined the centrosymmetric dimer of **1** (Fig. 4), which is stabilized by π-stacking involving both the aromatic and chelate rings. The analysis revealed that the monomers are interconnected by multiple bond critical points (depicted as magenta spheres) and bond paths (illustrated with dashed lines) (Fig. 6). These features characterize several C–H···N contacts and π-stacking interactions. Remarkably, the QTAIM analysis also identified the formation of two bifurcated tetrel bonds (Fig. 6). This arrangement resulted in a dimerization energy of −30.5 kcal mol^{-1}, underscoring the significant role of this intricate combination of interactions in the solid-state structure of **1**.

The QTAIM analysis of the self-assembled dimer of **2** revealed a total of 13 BCPs and bond paths interconnect both monomers, highlighting the intricate combination of interactions (Fig. 6). Most of the BCPs characterize π-stacking interactions. The QTAIM confirmed the existence of Pb···N(amine) tetrel bonds (Fig. 6). Additionally, C–H···O and C–H···π contacts are present, each characterized by a BCP and bond path linking an aromatic hydrogen atom of the non-coordinated pyridine ring to the oxygen atom of the hydrazido group (C–H···O) or to a carbon atom of the pyridine ring belonging to

 This journal is © the Partner Organisations 2024

Open Access Article. Published on 23 July 2024. Downloaded on 1/21/2026 11:43:33 PM.
This article is licensed under a Creative Commons Attribution 3.0 Unported Licence.

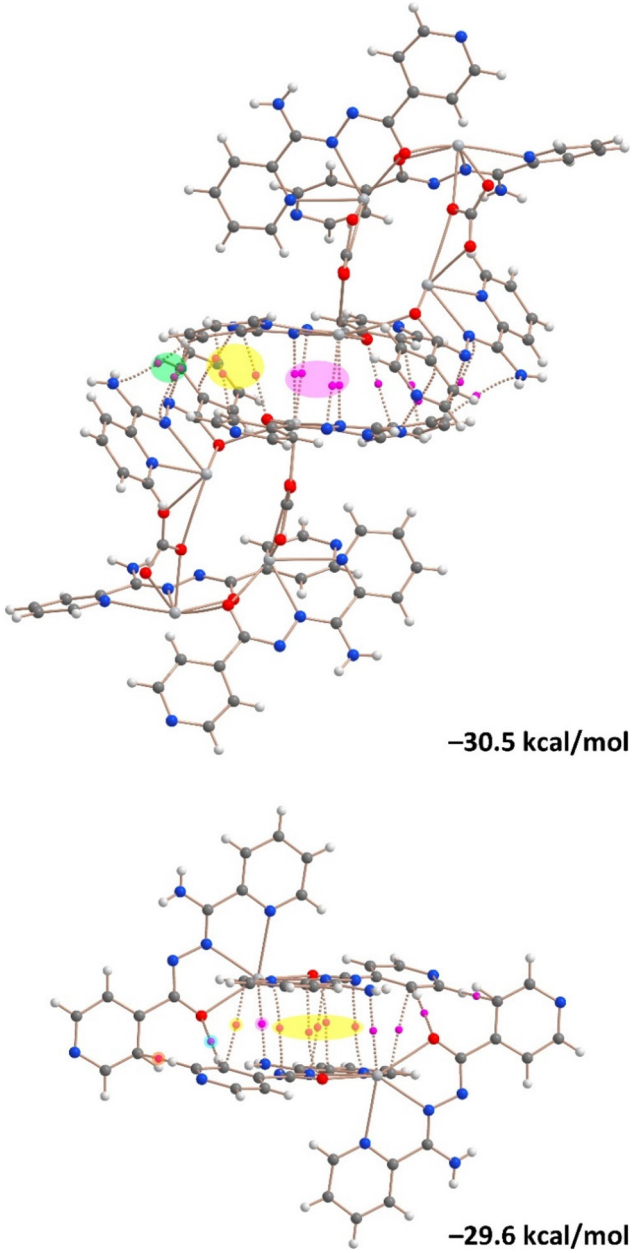

Fig. 6 QTAIM analysis of the dimers of **1** (top) and **2** (bottom) with the corresponding dimerization energies. Bond critical points are shown as magenta spheres and bond paths are depicted as dashed lines. Color code of the highlighted areas: Pb···N tetrel bond = magenta, π···π interaction = yellow, C–H···N interaction = green, C–H···O interaction = cyan, and C–H···π interaction = orange.

the adjacent monomer (C–H···π). The dimerization energy (−29.6 kcal mol^{-1}) was similar to that obtained for the dimer of **1** (Fig. 6), underscoring its significant role in the crystal packing of **2**.

Further investigations were carried out to understand the attractive and noncovalent nature of the Pb···N contacts in the self-assembled dimer of **1**. This was achieved using a combined 2D plot of the Laplacian of electron density ($\nabla^2\rho$) and 2D reduced density gradient (RDG) maps (Fig. 7). The $\nabla^2\rho$ 2D plot provides insights into the covalency of the interaction, while the RDG map effectively identifies regions of noncovalent interactions, making these combined maps highly useful for gaining a comprehensive understanding of the bonding characteristics. Additionally, the sign of the second eigenvalue of the Hessian matrix of $\nabla^2\rho$ (λ_2) within these low RDG regions indicated the presence of attractive forces, further confirming the nature of the bond. An electron localization function (ELF) 2D map was also utilized to delineate the nucleophilic and electrophilic regions within the tetrel-bonded dimer. This analysis provided insights into the electronic interactions and stability characteristics of the Pb···N tetrel bonds in the dimer (Fig. 7 and Table 3).

The 2D $\nabla^2\rho$ analysis showed positive values (represented by solid line isocontours) between the Pb and N atoms, illustrat-

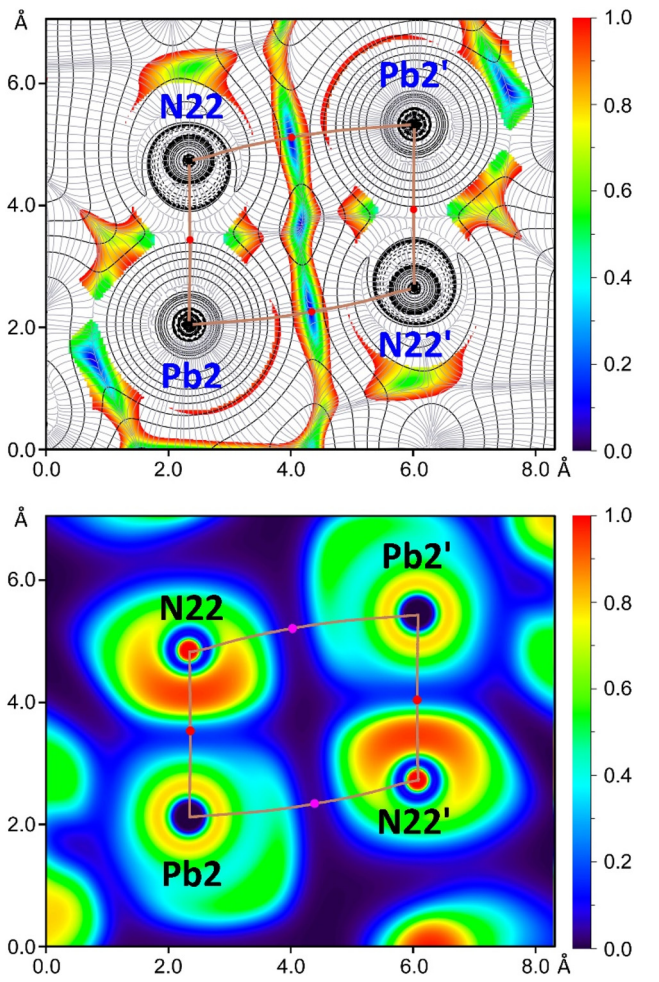

Fig. 7 (Top) 2D plot of the Laplacian (dashed and solid lines are for negative and positive values, respectively), including the gradient lines (in grey) overlapped with the 2D RDG map, and (bottom) the 2D ELF map for **1**. The 2D maps are represented in the plane defined by Pb2 and N22 atoms (symmetry code: −*x*, *y*, 1/2 − *z*). The bond paths are represented as brown lines, and BCPs of the coordination and tetrel bonds are shown as red and magenta dots, respectively. The RDG density cut-off is 0.05 a.u.

Table 3 QTAIM and ELF values (a.u.) for the BCPs, characterizing the coordination and tetrel bonds in **1** (symmetry code: 1/2 − *x*, *y*, −*z*)

BCP	$\rho(r)$	$G(r)$	$V(r)$	$\nabla^2\rho(r)$	ELF	λ_2
Pb2–N22	0.0605	0.0520	−0.0618	0.1691	0.209	−0.0027
Pb2···N22′	0.0096	0.0066	−0.0053	0.0313	0.035	−0.0062

Open Access Article. Published on 23 July 2024. Downloaded on 1/21/2026 11:43:33 PM. This article is licensed under a Creative Commons Attribution 3.0 Unported Licence.

ing both coordination bonds (Pb2–N22 and Pb2′–N22′) and tetrel bonds (Pb2···N22′ and Pb2′···N22). This distinction was further clarified by the 2D RDG map, which showed blue isocontours specifically in areas corresponding to the elongated Pb···N distances (tetrel bonds), effectively differentiating the coordination bonds from tetrel bonds. The BCPs and bond paths that denote tetrel bonds are coloured in magenta, where the RDG values are near zero (Fig. 7). The ELF 2D map added another level of detail, revealing the contrasting characteristics of Pb–N coordination and Pb···N tetrel bonds. It showed a peak in ELF for the lone pairs at the nitrogen atoms and underscores the electrophilic nature of the Pb atoms. Moreover, the map indicated that areas between the Pb and N atoms connected by coordination bonds are coloured blue (ELF = 0.21 at the BCP in red), suggesting some degree of electron localization indicative of electron sharing. Conversely, the regions associated with tetrel bonds, marked by magenta BCPs in areas of minimal electron density (depicted in black), underscore the typical features of noncovalent interactions. This visualization confirmed the weak noncovalent nature of the tetrel bonds.

The QTAIM and ELF parameters at the Pb···N BCPs characterize the tetrel bonds as weak (Table 3). This classification was supported by electron density (ρ) values below 0.010 a.u., positive and small values of the Laplacian of electron density ($\nabla^2\rho$), and the smaller absolute value of the potential energy density ($|V|$) compared to the kinetic energy density (G) at this BCP. Furthermore, the negative value of the second eigenvalue of the Hessian matrix (λ_2) indicates the presence of attractive forces. Comparative data highlight the strong differences between the tetrel and coordination bonds (Table 3). Specifically, in the coordination bond, the ρ is higher than 0.06 a.u. and the value of the total energy density is negative (H = G + V = –0.0098 a.u.), indicative of some degree of covalency. Moreover, the values of $\nabla^2\rho(r)$, ELF, and λ_2 are significantly higher for Pb2–N22, consistent with the coordination nature of this bond.

3. Conclusions

To sum up, we report the synthesis and detailed analysis of the novel tetranuclear complex $[Pb_4L_4(CO_3)_2]\cdot 4H_2O$ (**1**·$4H_2O$), which was fabricated from *N*′-isonicotinoylpicolinohydrazonamide (**HL**) by electrochemical oxidation of a lead anode in a CH_3CN:MeOH solution. The carbonate anions were directly formed from conversion of aerial carbon dioxide by the lead (II)–**L** complex system under electrochemical conditions, followed by its trapping in the structure of **1**. The same reaction but under a nitrogen atmosphere allowed obtaining the novel mononuclear complex $[PbL_2]\cdot MeOH\cdot 2H_2O$ (**2**·$MeOH\cdot 2H_2O$). In the molecular structure of complex **1**, both the ligands **L** and carbonate anions exhibit a tetradentate bridging coordination mode. In particular, the ligand **L** chelated the metal cation through the 2-pyridil and imine nitrogen atoms and carbonyl oxygen atom. The latter atom is also linked to the second metal cation, thus exhibiting a bridging bidentate coordination mode. In the carbonate anion, two oxygen atoms are linked to two neighbouring metal cations, while the third oxygen atom links the same metal two cations in a bridging bidentate coordination mode. The molecular structure of **1** is stabilized by a pair of Pb···O tetrel bonds formed with the bidentate oxygen atom of the carbonate anion, while molecules of **1** are interlinked through the reciprocal Pb···N tetrel bonds with the N–N fragments of the ligands **L**, yielding a 1D supramolecular chain. The resulting chain is further stabilized by π···π interactions formed between the 2- and 4-pyridil fragments of the ligands **L**. These chains are linked by the reciprocal N–H···O hydrogen bonds and π···π interactions. In the structure of **2**, each ligand **L** exhibits a tridentate coordination mode. The molecules of **2** are also interlinked through reciprocal π(chelate ring)···π(chelate ring), π(chelate ring) ···π(noncovalent ring), and Pb···π(noncovalent ring) interactions, similar to **1**, yielding a 1D supramolecular chain, which is, in turn, also stabilized by π(2-pyridyl)···π(4-pyridyl) interactions. The DFT study evidenced that the Pb···N tetrel bonds are stabilizing and, cooperatively with other interactions, contribute to the formation of the self-assembled dimers in **1** and **2**. Both complexes were found to be emissive in a solution of MeOH with a broad band from about 400 nm to 800 nm. The CIE-1931 chromaticity coordinates of (0.38, 0.37) and (0.31, 0.32) for **1**·$4H_2O$ and **2**·$MeOH\cdot 2H_2O$, respectively, fall within the white gamut of the chromaticity diagram.

4. Experimental

Materials and physical measurements

All the reagents and solvents were commercially available and used without further purification. **HL** was synthesized according to a recently described procedure.[40] The FTIR spectra in KBr pellets were obtained with a FT 801 spectrometer. The ^{1}H NMR spectra in DMSO-d_6 were recorded with a Bruker DPX FT/NMR-400 spectrometer. The absorption and fluorescence spectra were recorded from a freshly prepared solution of the complex in freshly distilled MeOH using a Jasco V-770 spectrophotometer and Edinburgh Instruments FS5 spectrofluoro-

 This journal is © the Partner Organisations 2024

Open Access Article. Published on 23 July 2024. Downloaded on 1/21/2026 11:43:33 PM. This article is licensed under a Creative Commons Attribution 3.0 Unported Licence.

meter, respectively. Elemental analysis was performed using a LECO-elemental analyzer.

Synthesis

The complex was obtained using an electrochemical procedure The cell consisted of a tall-form beaker (100 mL) fitted with a rubber bung through which the electrodes entered. An acetonitrile solution of **HL**, containing a few mg of $[N(CH_3)_4]ClO_4$ as a current carrier, was electrolyzed using platinum wire as the cathode and a metal plate as the sacrificial anode (**Caution!** *Although problems were not encountered in this work, all perchlorate compounds are potentially explosive, and should be handled in small quantities and with great care!*). The applied voltages (4–10 V) allowed sufficient current flow for smooth dissolution of the metal. The current was maintained at 5 mA for 1 h. During the electrolysis, hydrogen was evolved at the cathode. Under these conditions, the cell can be summarized as $Pb_{(+)}$/**HL** + $CH_3CN/Pt_{(-)}$.

1·4H$_2$O. Electrochemical oxidation of a lead anode under an ambient atmosphere in a solution of **HL** (0.048 g, 0.2 mmol) in CH_3CN : MeOH (1 : 1, 80 mL) at 7 V and 5 mA for 1 h caused 19 mg of lead to be dissolved, E_f = 0.50 mol F^{-1}. Yellow prism-like crystals, suitable for X-ray studies, were obtained by slow evaporation of the resulting solution. Yield: 93.6 mg (94.5%). Anal. calc. for $C_{50}H_{40}N_{20}O_{10}Pb_4$, 4($H_2O$) (1981.86): C 30.30, H 2.44 and N 14.13%; found: C 30.40, H 2.40 and N 14.11%.

2·MeOH·2H$_2$O. Electrochemical oxidation of a lead anode under a nitrogen atmosphere in a solution of **HL** (0.024 g, 0.1 mmol) in CH_3CN : MeOH (1 : 1, 80 mL) at 9 V and 5 mA for 0.5 h caused 10 mg of lead to be dissolved, E_f = 0.51 mol F^{-1}. Orange needle-like crystals, suitable for X-ray studies, were obtained by slow evaporation of the resulting solution. Yield: 34.7 mg (91.7%). Anal. calc. for $C_{24}H_{20}N_{10}O_2Pb$, CH_4O, 2(H_2O) (755.76): C 39.73, H 3.73 and N 18.53%; found: C 39.64, H 3.68 and N 18.58%.

X-Ray diffraction analysis

The X-ray diffraction data were collected at 100(2) K on a Bruker D8 VENTURE PHOTON III-14 diffractometer (Mo-Kα, λ = 0.71073 Å, graphite monochromator). The data were processed with APEX4[42] and corrected for absorption using SADABS.[43] The structure was solved by direct methods using the program SHELXS-2013[44] and refined by the full-matrix least-squares technique using SHELXL-2013.[44] All hydrogen atom positions were located on a difference map and included as fixed contributions riding on attached atoms with isotropic thermal parameters 1.2 times those of their carrier atoms.

Crystal data for 1·4H$_2$O. $C_{50}H_{40}N_{20}O_{10}Pb_4$, 4($H_2O$); M_r = 1981.84 g mol^{-1}, monoclinic, space group *I*2/*a*, *a* = 19.1999(8), *b* = 15.1198(7), *c* = 21.6170(14) Å, β = 106.184(1)°, *V* = 6026.7(5) $Å^3$, *Z* = 4, ρ = 2.184 g cm^{-3}, μ(Mo-Kα) = 11.220 mm^{-1}, reflections: 104 566 collected, 7479 unique, R_{int} = 0.051, R_1(all) = 0.0256, wR_2(all) = 0.0381, *S* = 1.047.

Crystal data for 2·MeOH·2H$_2$O. $C_{24}H_{20}N_{10}O_2Pb$, CH_4O, 2(H_2O); M_r = 755.76 g mol^{-1}, monoclinic, space group $P2_1/n$, *a* = 12.783(5), *b* = 11.084(3), *c* = 20.126(7) Å, β = 99.868(12)°, *V* = 2809.4(17) $Å^3$, *Z* = 4, ρ = 1.787 g cm^{-3}, μ(Mo-Kα) = 6.060 mm^{-1}, reflections: 78 795 collected, 6708 unique, R_{int} = 0.073, R_1(all) = 0.0330, wR_2(all) = 0.0448, *S* = 1.012.

Theoretical calculations

The geometries of the complexes were computed at the PBE0-D3/def2-TZVP level of theory,[45–47] using the crystallographic coordinates within the Gaussian-16 program.[48] The "atoms-in-molecules" (AIM)[49] analysis of the electron density was performed at the same level of theory using the AIMAII program.[50] The reduced density gradient (RDG)[51] and electron localization function (ELF)[52] 2D plots were computed using the Multiwfn program.[53] The QTAIM analysis was performed using the AIMAII program.[50] The Laplacian of electron density could be decomposed into the sum of contributions along the three principal axes of maximal variation, giving the three eigenvalues of the Hessian matrix (λ_1, λ_2, and λ_3). The sign of λ_2 could be utilized to distinguish bonding (attractive, $\lambda_2 < 0$) weak interactions from non-bonding ones (repulsive, $\lambda_2 > 0$).[51]

Data availability

All software packages utilized for the theoretical calculations are thoroughly described and appropriately cited in the Theoretical calculations section. X-ray coordinates were employed for the calculations and can be accessed from CIF files. Crystallographic data for compounds **1** and **2** have been deposited at the CCDC with accession numbers 2257285 and 2355288,† respectively. Additionally, CIF format crystallographic data have been included as ESI.†

Conflicts of interest

There are no conflicts to declare.

Acknowledgements

This work was supported by the grant from the Russian Science Foundation (No. 24-23-00118). We thank MICIU/AEI of Spain (PID2020-115637GB-I00, FEDER funds) for financial support. We thank the CTI (UIB) for computational facilities.

References

1 P. Falkowski, R. J. Scholes, E. Boyle, J. Canadell, D. Canfield, J. Elser, N. Gruber, K. Hibbard, P. Högberg, S. Linder, F. T. Mackenzie, B. Moore III, T. Pedersen, Y. Rosenthal, S. Seitzinger, V. Smetacek and W. Steffen, The Global Carbon Cycle: A Test of Our Knowledge of Earth as a System, *Science*, 2000, **290**, 291.
2 D. W. Keith, Why Capture CO_2 from the Atmosphere?, *Science*, 2009, **325**, 1654.

Open Access Article. Published on 23 July 2024. Downloaded on 1/21/2026 11:43:33 PM. This article is licensed under a Creative Commons Attribution 3.0 Unported Licence.

3 F. Parrenin, V. Masson-Delmotte, P. Köhler, D. Raynaud, D. Paillard, J. Schwander, C. Barbante, A. Landais, A. Wegner and J. Jouzel, Synchronous Change of Atmospheric CO_2 and Antarctic Temperature During the Last Deglacial Warming, *Science*, 2013, **339**, 1060.
4 P. G. Falkowski, R. T. Barber and V. Smetacek, Biogeochemical Controls and Feedbacks on Ocean Primary Production, *Science*, 1998, **281**, 200.
5 C. B. Field, M. J. Behrenfeld, J. T. Randerson and P. Falkowski, Primary Production of the Biosphere: Integrating Terrestrial and Oceanic Components, *Science*, 1998, **281**, 237.
6 T. Sakakura, J.-C. Choi and H. Yasuda, Transformation of Carbon Dioxide, *Chem. Rev.*, 2007, **107**, 2365.
7 J.-M. Savéant, Molecular Catalysis of Electrochemical Reactions. Mechanistic Aspects, *Chem. Rev.*, 2008, **108**, 2348.
8 C. Liu, T. R. Cundari and A. K. Wilson, Periodic Trends in 3d Metal Mediated CO_2 Activation, in *Applications of Molecular Modeling to Challenges in Clean Energy*, ed. G. Fitzgerald and N. Govind, 2013, ACS Symposium Series; American Chemical Society, Washington, DC, USA, p. 67.
9 E. Lamy, L. Nadjo and J. M. Savéant, Standard potential and kinetic parameters of the electrochemical reduction of carbon dioxide in dimethylformamide, *J. Electroanal. Chem.*, 1977, **78**, 403.
10 C. Amatore and J.-M. Saveant, Mechanism and kinetic characteristics of the electrochemical reduction of carbon dioxide in media of low proton availability, *J. Am. Chem. Soc.*, 1981, **103**, 5021.
11 H. A. Schwarz and R. W. Dodson, Reduction potentials of CO_2 and the alcohol radicals, *J. Phys. Chem.*, 1989, **93**, 409.
12 J. O. T. W, Hydrogen bonding : S.N. Vinogradov and R.H. Linnell, Van Nostrand Reinhold Company, London, 1971, pp. 319, price £4.75, *J. Mol. Struct.*, 1972, **14**, 470.
13 G. R. Desiraju, Reflections on the Hydrogen Bond in Crystal Engineering, *Cryst. Growth Des.*, 2011, **11**, 896.
14 S. J. Grabowski, Analysis of Hydrogen Bonds in Crystals, *Crystals*, 2016, **6**, 59.
15 C. A. Hunter and J. K. M. Sanders, The nature of π–π interactions, *J. Am. Chem. Soc.*, 1990, **112**, 5525.
16 K. Müller-Dethlefs and P. Hobza, Noncovalent Interactions: A Challenge for Experiment and Theory, *Chem. Rev.*, 2000, **100**, 143.
17 C. Janiak, A critical account on π–π stacking in metal complexes with aromatic nitrogen-containing ligands, *J. Chem. Soc., Dalton Trans.*, 2000, 3885.
18 T. Clark, M. Hennemann, J. S. Murray and P. Politzer, Halogen bonding: the σ-hole, *J. Mol. Model.*, 2007, **13**, 291.
19 Special Issue "Tetrel Bonds", **https://www.mdpi.com/journal/molecules/special_issues/Tetrel_Bonds**.
20 L. Shimoni-Livny, J. P. Glusker and C. W. Bock, Lone Pair Functionality in Divalent Lead Compounds, *Inorg. Chem.*, 1998, **37**, 1853.
21 A. Bauzá, T. J. Mooibroek and A. Frontera, Tetrel Bonding Interactions, *Chem. Rec.*, 2016, **16**, 473.
22 A. Bauzá, S. K. Seth and A. Frontera, Tetrel bonding interactions at work: Impact on tin and lead coordination compounds, *Coord. Chem. Rev.*, 2019, **384**, 107.
23 I. Alkorta, J. Elguero and A. Frontera, Not Only Hydrogen Bonds: Other Noncovalent Interactions, *Crystals*, 2020, **10**, 180.
24 G. Mahmoudi, A. Bauzá, M. Amini, E. Molins, J. T. Mague and A. Frontera, On the importance of tetrel bonding interactions in lead(II) complexes with (iso)nicotinohydrazide based ligands and several anions, *Dalton Trans.*, 2016, **45**, 10708.
25 G. Mahmoudi, A. V. Gurbanov, S. R. Hemida, R. Corballo, M. Amini, A. Bacchi, M. P. Mitoraj, F. Sagan, M. Kukulka and D. A. Safin, Ligand-Driven Coordination Sphere-Induced Engineering of Hybride Materials Constructed from $PbCl_2$ and Bis-Pyridyl Organic Linkers for Single-Component Light-Emitting Phosphors, *Inorg. Chem.*, 2017, **56**, 9698.
26 G. Mahmoudi, A. A. Khandar, J. White, M. P. Mitoraj, H. S. Jena, P. Van Der Voort, N. Qureshi, A. M. Kirillov, K. Robeyns and D. A. Safin, Polar protic solvent-trapping polymorphism of the Hg^{II}-hydrazone coordination polymer: experimental and theoretical findings, *CrystEngComm*, 2017, **19**, 3017.
27 G. Mahmoudi, D. A. Safin, M. P. Mitoraj, M. Amini, M. Kubicki, T. Doert, F. Locherere and M. Fleck, Anion-driven tetrel bond-induced engineering of lead(II) architectures with *N′*-(1-(2-pyridyl)ethylidene)nicotinohydrazide: experimental and theoretical findings, *Inorg. Chem. Front.*, 2017, **4**, 171.
28 G. Mahmoudi, E. Zangrando, M. P. Mitoraj, A. V. Gurbanov, F. I. Zubkov, M. Moosavifar, I. A. Konyaeva, A. M. Kirillov and D. A. Safin, Extended lead(II) architectures engineered *via* tetrel bonding interactions, *New J. Chem.*, 2018, **42**, 4959.
29 G. Mahmoudi, F. A. Afkhami, A. Kennedy, F. I. Zubkov, E. Zangrando, A. M. Kirillov, E. Molins, M. P. Mitoraj and D. A. Safin, Lead(II) coordination polymers driven by pyridine-hydrazine donors: from anion-guided self-assembly to structural features, *Dalton Trans.*, 2020, **49**, 11238.
30 F. A. Afkhami, G. Mahmoudi, F. Qu, A. Gupta, M. Köse, E. Zangrando, F. I. Zubkov, I. Alkorta and D. A. Safin, Supramolecular lead(II) architectures engineered by tetrel bonds, *CrystEngComm*, 2020, **22**, 2389.
31 G. Mahmoudi, M. Abedi, S. E. Lawrence, E. Zangrando, M. G. Babashkina, A. Klein, A. Frontera and D. A. Safin, Tetrel Bonding and Other Non-Covalent Interactions Assisted Supramolecular Aggregation in a New Pb(II) Complex of an Isonicotinohydrazide, *Molecules*, 2020, **25**, 4056.
32 G. Mahmoudi, F. A. Afkhami, E. Zangrando, W. Kaminsky, A. Frontera and D. A. Safin, A supramolecular 3D structure constructed from a new metal chelate self-assembled from $Sn(NCS)_2$ and phenyl(pyridin-2-yl)methylenepicolinohydrazide, *J. Mol. Struct.*, 2020, **49**, 129188.

 This journal is © the Partner Organisations 2024

Open Access Article. Published on 23 July 2024. Downloaded on 1/21/2026 11:43:33 PM. This article is licensed under a Creative Commons Attribution 3.0 Unported Licence.

33 G. Mahmoudi, M. Kubicki, D. Choquesillo-Lazarte, B. Miroslaw, E. V. Alexandrov, P. N. Zolotarev, A. Frontera and D. A. Safin, Supramolecular architectures of $Mn(NCS)_2$ complexes with *N'*-(1-(pyridin-4-yl)ethylidene)picolinohydrazide and *N'*-(phenyl(pyridin-4-yl)methylene)isonicotinohydrazide, *Polyhedron*, 2020, **190**, 114776.

34 F. A. Afkhami, G. Mahmoudi, F. Qu, A. Gupta, E. Zangrando, A. Frontera and D. A. Safin, Supramolecular architecture constructed from the hemidirected lead(II) complex with *N'*-(4-hydroxybenzylidene)isonicotinohydrazide, *Inorg. Chim. Acta*, 2020, **502**, 119350.

35 J. D. Velásquez, G. Mahmoudi, E. Zangrando, B. Miroslaw, D. A. Safin and J. Echeverría, Non-covalent interactions induced supramolecular architecture of $Hg(NCS)_2$ with 3-pyridinecarbaldehyde nicotinoylhydrazone, *Inorg. Chim. Acta*, 2020, **509**, 119700.

36 G. Mahmoudi, A. Masoudiasl, F. A. Afkhami, J. M. White, E. Zangrando, A. V. Gurbanov, A. Frontera and D. A. Safin, A new coordination polymer constructed from $Pb(NO_3)_2$ and a benzylideneisonicotinohydrazide derivative: Coordination-induced generation of a π-hole towards a tetrel-bonding stabilized structure, *J. Mol. Struct.*, 2021, **1234**, 130139.

37 I. Garcia-Santos, A. Castiñeiras, G. Mahmoudi, M. G. Babashkina, E. Zangrando, R. M. Gomila, A. Frontera and D. A. Safin, Supramolecular aggregation of lead(II) perchlorate and a thiosemicarbazide derivative linked by a myriad of non-covalent interactions, *Inorg. Chim. Acta*, 2022, **538**, 120974.

38 G. Mahmoudi, I. Garcia-Santos, M. Pittelkow, F. S. Kamounah, E. Zangrando, M. G. Babashkina, A. Frontera and D. A. Safin, The tetrel bonding role in supramolecular aggregation of lead(II) acetate and a thiosemicarbazide derivative, *Acta Crystallogr.*, 2022, **B78**, 685.

39 I. Garcia-Santos, A. Castiñeiras, G. Mahmoudi, M. G. Babashkina, E. Zangrando, R. M. Gomila, A. Frontera and D. A. Safin, An extended supramolecular coordination compound produced from $PbCl_2$ and *N'*-isonicotinoylpicolinohydrazonamide, *CrystEngComm*, 2022, **24**, 368.

40 I. Garcia-Santos, A. Castiñeiras, B. Eftekhari Sis, G. Mahmoudi and D. A. Safin, *N'*-isonicotinoylpicolinohydrazonamide: Synthesis, crystal structure, DFT and ADMET studies, and in silico inhibition properties toward a series of COVID-19 proteins, *Polyhedron*, 2023, **235**, 116362.

41 C. P. Frizzo and M. A. P. Martins, Aromaticity in heterocycles: new HOMA index parametrization, *Struct. Chem.*, 2012, **23**, 375.

42 *APEX4 Software, v2021.10-0*, Bruker AXS Inc., Madison, Wisconsin, USA, 2021.

43 G. M. Sheldrick, *SADABS*, Bruker AXS Inc., Madison, WI-53719, USA, 1997.

44 G. M. Sheldrick, A short history of SHELX, *Acta Crystallogr.*, 2008, **A64**, 112.

45 C. Adamo and V. Barone, Toward reliable density functional methods without adjustable parameters: The PBE0 model, *J. Chem. Phys.*, 1999, **110**, 6158.

46 F. Weigend, Accurate Coulomb-fitting basis sets for H to Rn, *Phys. Chem. Chem. Phys.*, 2006, **8**, 1057.

47 E. Caldeweyher, C. Bannwarth and S. Grimme, Extension of the D3 dispersion coefficient model, *J. Chem. Phys.*, 2017, **147**, 034112.

48 M. J. Frisch, G. W. Trucks, H. B. Schlegel, G. E. Scuseria, M. A. Robb, J. R. Cheeseman, G. Scalmani, V. Barone, G. A. Petersson, H. Nakatsuji, X. Li, M. Caricato, A. V. Marenich, J. Bloino, B. G. Janesko, R. Gomperts, B. Mennucci, H. P. Hratchian, J. V. Ortiz, A. F. Izmaylov, J. L. Sonnenberg, D. Williams-Young, F. Ding, F. Lipparini, F. Egidi, J. Goings, B. Peng, A. Petrone, T. Henderson, D. Ranasinghe, V. G. Zakrzewski, J. Gao, N. Rega, G. Zheng, W. Liang, M. Hada, M. Ehara, K. Toyota, R. Fukuda, J. Hasegawa, M. Ishida, T. Nakajima, Y. Honda, O. Kitao, H. Nakai, T. Vreven, K. Throssell, J. A. Montgomery Jr., J. E. Peralta, F. Ogliaro, M. J. Bearpark, J. J. Heyd, E. N. Brothers, K. N. Kudin, V. N. Staroverov, T. A. Keith, R. Kobayashi, J. Normand, K. Raghavachari, A. P. Rendell, J. C. Burant, S. S. Iyengar, J. Tomasi, M. Cossi, J. M. Millam, M. Klene, C. Adamo, R. Cammi, J. W. Ochterski, R. L. Martin, K. Morokuma, O. Farkas, J. B. Foresman and D. J. Fox, *Gaussian 16, Revision C.01*, Gaussian, Inc., Wallingford CT, 2016.

49 R. F. W. Bader, A quantum theory of molecular structure and its applications, *Chem. Rev.*, 1991, **91**, 893.

50 A. Todd and T. K. Keith, *AIMAll (Version 19.10.12)*, Gristmill Software, Overland Park KS, USA, 2019 (aim.tkgristmill.com).

51 J. Contreras-Garcia, E. R. Johnson, S. Keinan, R. Chaudret, J.-P. Piquemal, D. N. Beratan and W. Yang, NCIPLOT: A Program for Plotting Noncovalent Interaction Regions, *J. Chem. Theory Comput.*, 2011, **7**, 625.

52 A. D. Becke and K. E. Edgecombe, A simple measure of electron localization in atomic and molecular systems, *J. Chem. Phys.*, 1990, **92**, 5397.

53 T. Lu and F. Chen, Multiwfn: A multifunctional wavefunction analyzer, *J. Comput. Chem.*, 2012, **33**, 580.